J. Fluid Mech. (2006), *vol.* 559, *pp.* 355–378.
doi:10.1017/S0022112006000395 Printed in the United Kingdom

Dynamics of driven liquid films on heterogeneous surfaces

By Y. ZHAO AND J. S. MARSHALL

Department of Mechanical & Industrial Engineering and IIHR – Hydroscience and Engineering, University of Iowa, Iowa City, IA 52242, USA

(Received 4 April 2005 and in revised form 4 January 2006)

A computational study is reported of the instability and growth of fingers for liquid films driven over heterogeneous surfaces. Computations are performed using a variation of the precursor-film model, in which a disjoining pressure term is used to introduce variation in the static contact angle, which in turn models surface heterogeneity. The formulation is shown to yield results consistent with the Tanner–Hoffman–Voinov dynamic contact angle formula for sufficiently small values of the precursor film thickness. A modification of the disjoining pressure coefficient is introduced which yields correct variation of dynamic contact angle for finite values of the precursor film thickness. The fingering instability is examined both for cases with ordered strips of different static contact angle and for cases with random variation in static contact angle. Surface heterogeneity is characterized by strip width and amplitude of static contact angle variation for the case with streamwise strips and by correlation length and variance of the static contact angle variation from its mean value for the random distribution case.

1. Introduction

The dynamics of driven liquid films is of interest in a wide variety of applications, including surface coating, printing and cleaning processes, biofilm transport within mammalian lungs, icing and aerodynamics of airplane wings, and reaction and transport of surface-active materials. Fingering instability and subsequent formation of rivulets from driven liquid films has consequently been the subject of a large literature in the past two decades. Numerous experiments have been reported for films driven by a body force, such as gravity or centrifugal force (Huppert 1982; Melo, Joanny & Fauve 1989; de Bruyn 1992; Fraysse & Homsy 1994; Hocking, Debler & Cook 1999; Johnson *et al.* 1999), or by a shear stress, such as wind shear or Marangoni force (Cazabat *et al.* 1990; Thompson & Marrochello 1999). The stability theory for finger growth on the driven film, originally developed by Troian *et al.* (1989), has been expanded for cases with normal body force on the substrate surface (Bertozzi & Brenner 1997), various film driving forces (Kataoka & Troian 1997), weak nonlinear effects (Kalliadasis 2000), weak inertial effects (López, Miksis & Bankoff 1997), presence of van der Waals forces (Golovin, Rubinstein & Pismen 2001), and non-uniform ambient film thickness (Davis & Troian 2003). Nonlinear computations have been reported that investigate the subsequent rivulet shape formed from these unstable fingers and the effect on the rivulet shape of factors such as normal body force (Moyle, Chen & Homsy 1999; Eres, Schwartz & Roy 2000; Diez & Kondic 2001; Kondic & Diez 2001). It was shown theoretically by Grigoriev (2003), and

experimentally by Garnier, Grigoriev & Schatz (2003), that the fingering instability can be suppressed by use of feedback control using thermal manipulation of the film.

Two different methods are frequently used in theoretical and computational work to regulate the singularity at the moving contact line – local slip near the contact line and introduction of a precursor film in front of the contact line. Spaid & Homsy (1996) compare results using the precursor film approach and a local slip approach and show that the theoretical fingering instability predictions are not sensitive to the method used to remove the contact-line singularity. Davis & Troian (2004) show that predictions for both modal and non-modal linear stability analyses for shear-driven films yield the same film profiles and dispersion curves for cases with precursor film and local slip regularization of the singularity. Moyle *et al.* (1999) report nonlinear computations with the local slip approach which indicate that the rivulet shape is not sensitive to the value of the slip parameter and that the computed rivulet shape using both simple local slip and precursor film models is in good agreement with experimental results. However, a comparison study by Diez, Kondic & Bertozzi (2000) shows that the precursor film method is more computationally efficient than the local slip method since it yields a stable computation with much larger values of the time step.

The vast majority of the literature on driven liquid films deals with homogeneous surfaces, whereas real surfaces exhibit a variety of heterogeneities, caused by variation in chemical composition (e.g. due to surface oil deposition) or surface roughness, which lead to spatial variation in static contact angle. The literature dealing with film dynamics on heterogeneous surfaces is sparse compared to that for homogeneous surfaces. An early study that examined the effect of variation in static contact angle on thin-film flows is reported by Greenspan (1978), who used the lubrication theory with local slip near the contact line to model motion of small droplets on surfaces with variable static contact angle. Greenspan reports that the advancing contact line is drawn toward regions with smaller contact angle and recedes from regions with relatively greater contact angle. Schwartz (1998) proposed that the precursor film method can be used to study problems with variable static contact angle by addition of a disjoining pressure at the liquid–gas interface, where the coefficient of the disjoining pressure is related to the local static contact angle. As discussed by de Gennes (1985), the disjoining pressure is related to van der Waals forces and other forces that occur when two surfaces are positioned close to each other. Schwartz (1998) then used this model to investigate the effect of static contact angle variation on droplet hysteresis by simulating a spreading droplet over an array of contamination 'spots', modelled by regions of variable static contact angle. Because this work was concerned with contact angle hysteresis, the contamination spots were selected to be relatively small, with contamination spot radius measuring approximately 5 %, and spot separation distance approximately 40 %, of the upstream liquid-layer thickness. Because of the small length scales used in the study, no rivulet formation due to the surface heterogeneity was observed. A similar numerical model was used by Schwartz & Eley (1998) to examine the bifurcation of a droplet placed on a surface with strong contact angle variation.

The disjoining pressure term developed by Schwartz (1998) was used by Marshall & Wang (2005) in a study of the effect of surface heterogeneity on fingering of a driven liquid film. Simulations of passage of a driven film front over isolated contamination spots of various sizes indicate that finger development is predicted well by the growth rate and length scale of the fastest-growing perturbation from the linear theory. However, in the case of an array of contamination spots, the spot separation distance

can impose a certain wavelength on the finger-like film perturbations. Several cases are recorded where the driven film exhibits large-scale finger growth as the front passes through an array of spots under conditions (length scale or normal gravity condition) for which the film front is stable according to linear stability theory.

For natural surfaces, contamination and roughness variation occur not in ordered arrays, but rather in a random manner. The current study builds on the work of Marshall & Wang (2005) by examining finger development on a driven film for heterogeneous surfaces, both with static contact angle set according to a random function, which is parameterized by the correlation length and variance of the static contact angle relative to its mean value, and with an ordered static contact angle variation along strips that are aligned with the flow. The case with random static contact angle might model the effects of surface contaminants in natural materials, whereas the case with ordered static contact angle variation on strips might be typical of an engineered material specifically intended to control the fingering instability. Related engineered surfaces were introduced in a computational study by Kondic & Diez (2002), who examined the effect of grooves in the substrate surface on the fingering instability, and in an experimental study by Kataoka & Troian (1999), who examined the effect of surface heating along vertical strips on the fingering instability for a film driven by thermal-induced surface tension gradients.

The paper is organized as follows. Section 2 gives a summary of the theory and computational method used in the study. Section 3 provides a detailed validation for the use of disjoining pressure as a method for setting static contact angle by comparing predictions of the method with the Tanner–Hoffman–Voinov (THV) formula for dynamic contact angle with different values of the precursor film thickness (Hoffman 1975; Voinov 1976; Tanner 1979). We note that although reasonable predictions seem to have been obtained by previous studies using disjoining pressure in precursor film models for problems with variable static contact angle, a detailed validation study of this method has not previously been reported. We also propose an extension of the disjoining pressure model in this section to yield results that are consistent with the THV formula for finite values of the precursor film thickness. Section 4 examines the fingering instability for problems with streamwise strips of different static contact angle. Section 5 examines the effect of the correlation length scale on fingering instability and rivulet formation for problems with random static contact angle variation. Conclusions are given in § 6.

2. Computational model

2.1. *Governing equations and solution method*

The current numerical study employs the lubrication theory, which assumes low film Reynolds number and small interface slope. Integrating the Stokes equation over the width of a liquid layer with thickness $h(\boldsymbol{x}, t)$ and making use of the small slope approximation yields an expression for the liquid flow rate vector $\boldsymbol{Q}$ tangent to the substrate surface as

$$\boldsymbol{Q} = -\frac{h^3}{3\mu}(\nabla \hat{p} - \rho g\, \boldsymbol{e}_x), \tag{1}$$

where $\hat{p}$ is the liquid pressure at the top surface of the layer, ρ and μ are the liquid density and viscosity, respectively, $\boldsymbol{e}_x$ is the base vector in the direction of front motion along the plate, g is the acceleration due to gravity, oriented tangent to the substrate (the x-direction), and $h(x, y, t)$ is the layer thickness. It is assumed

that the substrate surface is vertical, so that there is no component of gravitational force normal to the substrate. Substitution of (1) into the depth-integrated continuity equation $\partial h/\partial t = -\nabla \cdot \boldsymbol{Q}$ yields the governing equation for liquid layer thickness as

$$\frac{\partial h}{\partial t} = \nabla \cdot \left\{ \frac{h^3}{3\mu} [\nabla \hat{p} - \rho g \, \boldsymbol{e}_x] \right\}. \tag{2}$$

The liquid upper-surface pressure can be written as a sum of a capillary pressure and an additional *disjoining pressure* term, $-\Pi$, as

$$\hat{p} = -\sigma \nabla^2 h - \Pi, \tag{3}$$

where σ is the surface tension. An expression for Π is given in terms of the ratio of liquid layer thickness to the constant thickness h^* of the precursor film by (de Gennes 1985; Schwartz 1998)

$$\Pi = B \left[\left(\frac{h^*}{h} \right)^n - \left(\frac{h^*}{h} \right)^m \right], \tag{4}$$

where B, m and n are constants such that $n > m > 1$. The disjoining pressure, $-\Pi$, is negative for $h/h^* < 1$ and positive for $h/h^* > 1$, so that the layer thickness is always forced toward the specified precursor film thickness. This effect becomes small for $h/h^* \gg 1$. The stability condition for the precursor film requires that $-(\mathrm{d}\Pi/\mathrm{d}h)(h^*) = (n-m)B/h^* > 0$, which is satisfied for all positive values of the coefficient B. The disjoining pressure is related to a variety of additional forces that arise when two surfaces are brought in close contact with each other, including van der Waals and double-layer forces (de Gennes 1985). Van der Waals forces exhibit a retarded regime for sufficiently small layer thickness, in which $\Pi \propto h^{-4}$, and a non-retarded regime for larger film thicknesses, in which $\Pi \propto h^{-3}$ (de Gennes 1985). Double-layer and other short-range interfacial forces exhibit disjoining pressure variation with smaller powers of h, such as h^{-2} or h^{-1} (Mohanty 1981). Most previous computational studies have used $(n, m) = (3, 2)$ owing in part to the good numerical stability properties exhibited by this choice.

An expression for the constant B in (4) in terms of the static contact angle θ_E was derived by Schwartz (1998) using a control-volume analysis near the contact line as

$$B = \frac{(n-1)(m-1)}{h^*(n-m)} \sigma (1 - \cos\theta_E). \tag{5}$$

We show in § 3 that the result (5) is valid for infinitesimally small precursor film thicknesses, such that $h^* \ll h_\infty$, but leads to significant deviation from the known dynamic contact angle law for finite values of the dimensionless precursor film thickness $\delta \equiv h^*/h_\infty$ (e.g. for $\delta = O(0.01)$). A modified expression for the B coefficient is derived in § 3 which yields the correct variation of dynamic contact angle with static contact angle for $\delta \leqslant 0.1$.

We note that, as is common in computation of thin-film flows, the computational precursor film thickness is often much larger than that of the physical precursor film. In such cases, the precursor film is used more as a numerical device to regulate the moving contact-line singularity in computation of the macroscopic film motion than as a physically accurate model of the microscale processes at the scale of the physical precursor film. Similarly, although the expression for disjoining pressure resembles that resulting from van der Waals and double-layer forces, its usage in the current work is more as a numerical device to set the static contact angle within the context of the precursor-film model.

We consider a constant flow rate condition in which the layer thickness approaches a constant value h_∞ far upstream, which provides a characteristic length scale in the normal (z) direction. The characteristic length scale in the (x, y)-plane tangent to the substrate is denoted by L and the characteristic time scale is denoted by $T = L/U$, where U is the characteristic contact-line translation speed. Dimensionless variables are defined as

$$\left.\begin{aligned} &h' = h/h_\infty, \quad x' = x/L, \quad y' = y/L, \quad t' = t/T, \\ &\Pi' = \Pi h_\infty/\sigma\delta^{m-1}, \quad U' = TU/L. \end{aligned}\right\} \tag{6}$$

We set the tangential length scale L so as to balance the capillary term and the driving gravity term in the governing equation for h, which yields $\varepsilon^3 = Bo$, where $Bo = h_\infty^2 \rho g/\sigma$ is the Bond number and $\varepsilon \equiv h_\infty/L$ is the length-scale aspect ratio. The horizontal length and velocity scalings become $L = (\sigma h_\infty/\rho g)^{1/3}$ and $L/T = \rho g h_\infty^2/3\mu$. Substituting (3)–(6) into (2), the dimensionless equation for the liquid-layer thickness is

$$\frac{\partial h}{\partial t} = -\nabla \cdot \left\{ h^3 \nabla(\nabla^2 h) + \frac{\delta^{m-1}}{\varepsilon^2} h^3 \nabla \Pi + h^3 \boldsymbol{e}_x \right\}, \tag{7}$$

where for convenience, we have dropped the primes on the dimensionless variables.

Nonlinear computations of liquid-layer evolution are performed by solving (7) using a second-order ADI method similar to that reported by Witelski & Bowen (2003) for the lubrication equation. The computations are performed on a rectangular grid spanning the interval (x_{min}, x_{max}) and (y_{min}, y_{max}) with uniform grid spacing and subject to boundary conditions in the x-direction of the form

$$h(x_{min}, y) = 1, \quad h_x(x_{min}, y) = 0, \quad h(x_{max}, y) = \delta, \quad h_x(x_{max}, y) = 0. \tag{8a}$$

The boundary conditions in the y-direction are taken in § 4 to be periodic and in § 5 to be of the homogeneous form

$$h_y(x, y_{min}) = 0, \quad h_{yy}(x, y_{min}) = 0, \quad h_y(x, y_{max}) = 0, \quad h_{yy}(x, y_{max}) = 0. \tag{8b}$$

2.2. *Equilibrium solution and linear stability*

An equilibrium solution $h_0(x - Ut)$ for the liquid-layer thickness is obtained from (7) using the convected coordinate $\xi \equiv x - Ut$, where the dimensionless contact-line advection speed is obtained as

$$U = (1 - \delta^3)/(1 - \delta). \tag{9}$$

Results for the equilibrium layer thickness in gravity-driven flow with $\delta = 0.05$ are shown in figure 1(a) for cases with values of the static contact angle of $\theta_E = 0$ and 0.2. There exists a 'ridge' in the liquid-layer thickness just before the front, measuring about 40 % of the upstream liquid-layer thickness for the case with $\theta_E = 0$ and about 50 % of the upstream layer thickness for the case with $\theta_E = 0.2$.

Stability of the equilibrium solution is examined for perturbations that are periodic in the spanwise (y) direction, such that the layer thickness is given by

$$h(x, y, t) = h_0(\xi) + G(\xi, t) \exp(\mathrm{i}ky), \tag{10}$$

where k is the spanwise perturbation wavenumber. Substituting (10) into (7) and linearizing gives a fourth-order differential equation for the perturbation amplitude $G(\xi, t)$, which is subject to the boundary condition that the perturbations die away far upstream and far downstream of the front, or G, $G_\xi \to 0$ as $\xi \to \pm\infty$. This equation is solved numerically for $G(\xi, t)$ using a second-order Crank–Nicolson method similar

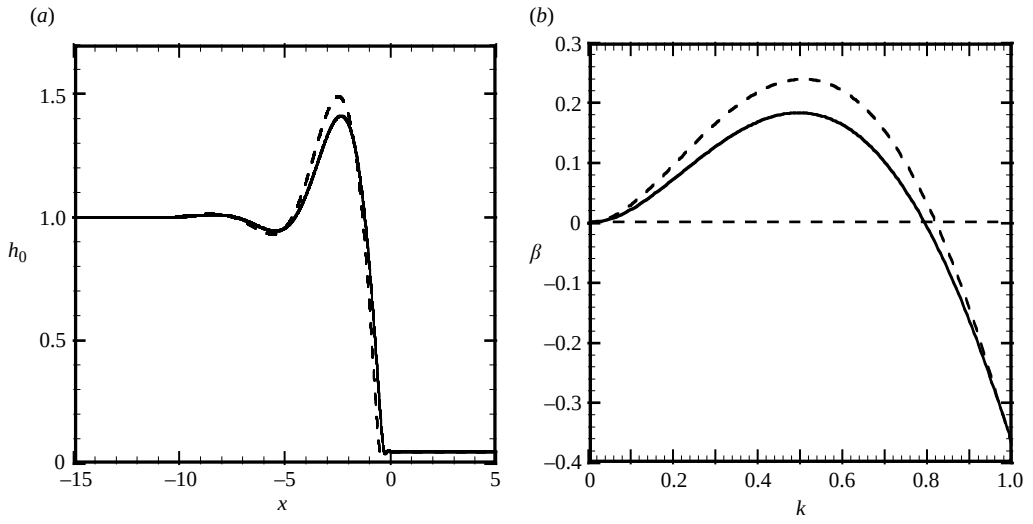

FIGURE 1. The effect of static contact angle on (*a*) equilibrium film thickness profile and (*b*) instability growth rate β as a function of wavenumber k for a case with $\delta = 0.05$ and static contact angle $\theta_E = 0$ (solid curve) and 0.2 (dashed-dotted curve).

to that employed for solving for the equilibrium layer profile $h_0(\xi)$. After the initial transient dies away, the computed perturbation amplitude is found to approach a separable form $G(\xi, t) \rightarrow A(\xi)e^{\beta t}$, where $A(\xi)$ specifies the spatial form of the eigenfunction and β is the growth rate corresponding to perturbations with spanwise wavenumber k. In the reported linear stability computations, we set the computational domain as $(-50, 10)$, with the front occurring at $x = 0$, and the space and time step as $\Delta x = 0.0017$ and $\Delta t = 0.005$. Tests with a grid with half as many points ($\Delta x = 0.0034$) and with various different values of Δt and x_{min} indicate that the root-mean-square uncertainty in the instability growth rate is less than 0.007, with the greatest sensitivity due to variation in Δx.

The computed perturbation growth rate β is plotted in figure 1(*b*) as a function of wavenumber for cases with precursor film thickness $\delta = 0.05$ with static contact angle $\theta_E = 0$ and 0.2. (For the $\theta_E = 0.2$ case, we use the modified disjoining pressure coefficient B given in (18) and (20).) The liquid-layer front is unstable for dimensionless wavenumbers below a critical value of $k_{crit} = 0.80$, with the most unstable waves corresponding to a wavenumber of $k_{max} = 0.48$. In agreement with Davis & Troian (2003), we observe an increase in both the peak equilibrium film thickness and the perturbation growth rate as the contact angle is increased.

3. Validation for dynamic contact angle

3.1. *Relationship between static and dynamic contact angles*

In this section, we seek to validate our computational model by examining the extent to which the disjoining pressure expression, (4), together with expression (5) for the coefficient B, yield predictions for the dynamic contact angle that are consistent with the well-known Tanner–Hoffman–Voinov (THV) formula (Hoffman 1975; Voinov 1976; Tanner 1979). This validation study is performed using a series of two-dimensional computations with different values of static contact angle θ_E, Bond number Bo, and precursor film thickness δ. Both our computations and the experiments of Tanner

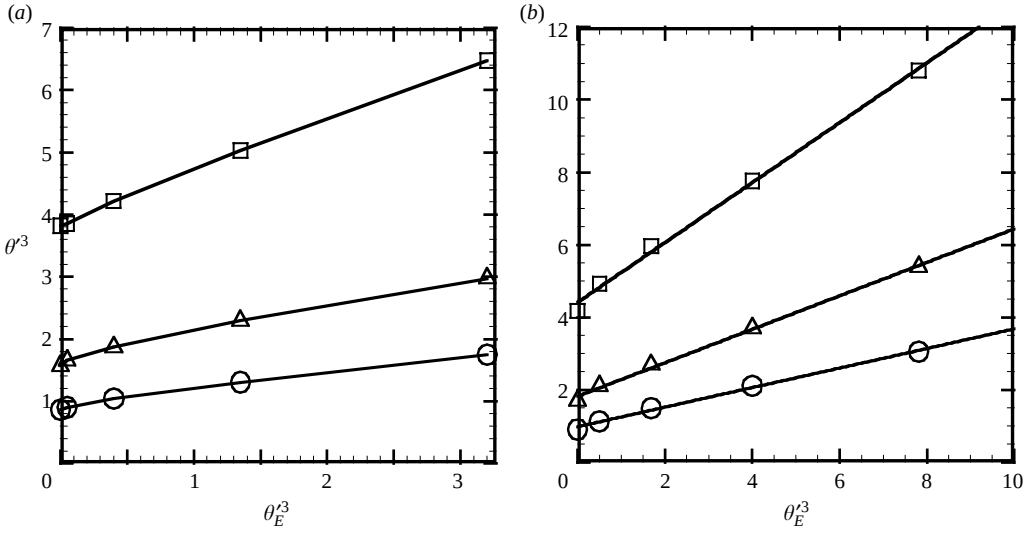

FIGURE 2. The cube of the dynamic contact angle versus the cube of the static contact angle for cases with precursor film thickness □, $\delta = 0.01$; △, 0.05; ○, 0.1, for (*a*) $Bo = 0.02$ and (*b*) $Bo = 0.002$.

(1979) and Hoffman (1975) deal with situations where the contact line is always advancing, such that the data are not affected by contact-line hysteresis. The computed contact angle in these computations is determined by fitting a straight line to the part of the film thickness curve with greatest slope near the region where the film meets the precursor film. The computed results for dynamic contact angle are compared to the THV formula, given by

$$\theta^3 = \theta_E^3 + D\mu U/\sigma, \tag{11}$$

where D is a constant and U is the contact-line velocity. Defining a scaled contact angle by $\theta' \equiv \theta/\varepsilon$ and using the non-dimensionalization (6) with $\varepsilon^3 = Bo$ and the equilibrium solution (9) for U, we can rewrite (11) in the dimensionless form

$$\theta'^3 = C\left[\theta_E'^3 + A(1-\delta^3)/(1-\delta)\right], \tag{12}$$

where A and C are constants, such that $C = 1$ in the THV formula.

It is found in all cases examined that the cube of the computed dynamic contact angle, θ'^3, varies nearly linearly with the cube of the static contact angle, $\theta_E'^3$. Examples of this linear relationship are shown in figure 2 for different values of the precursor film thickness and for Bond numbers of $Bo = 0.02$ and 0.002. The slope of the best-fit linear relationship is determined by data regression. The effect of grid increment Δx on the computed slope C in (12) is estimated by performing a series of computations for a case with $\delta = 0.01$ for different values ofΔx. Results from this grid resolution test, shown in figure 3, indicate that the solutions for slope C are converged to within 3.6 % of the asymptotic value for cases with $\delta/\Delta x \geqslant 1.5$. A similar result is obtained for tests with different values of δ. All computations with $\delta \geqslant 0.01$ reported in the remainder of this section are performed with $\Delta x = 0.0067$, which corresponds to $\delta/\Delta x \geqslant 1.5$. Computations with $\delta = 0.005$ are performed with the finer grid increment $\Delta x = 0.0033$, which corresponds to $\delta/\Delta x = 1.5$.

The slope C is plotted as a function of precursor film thickness in figure 4(*a*) for Bond numbers of 0.02 and 0.002. The predicted slopes C for the two different Bond

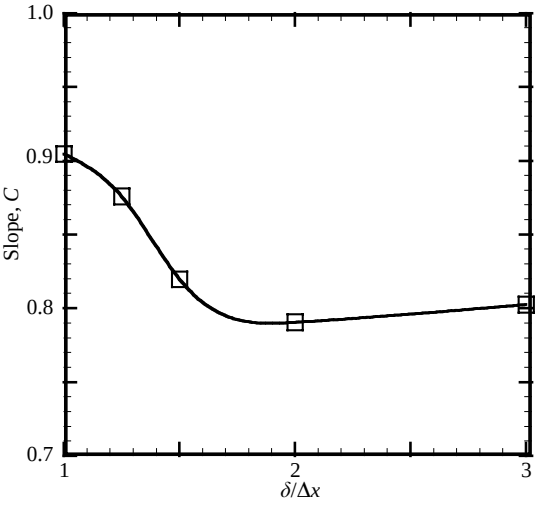

FIGURE 3. The effect of grid increment Δx on the computed slope C in (12) for a case with $\delta = 0.01$ for $Bo = 0.02$.

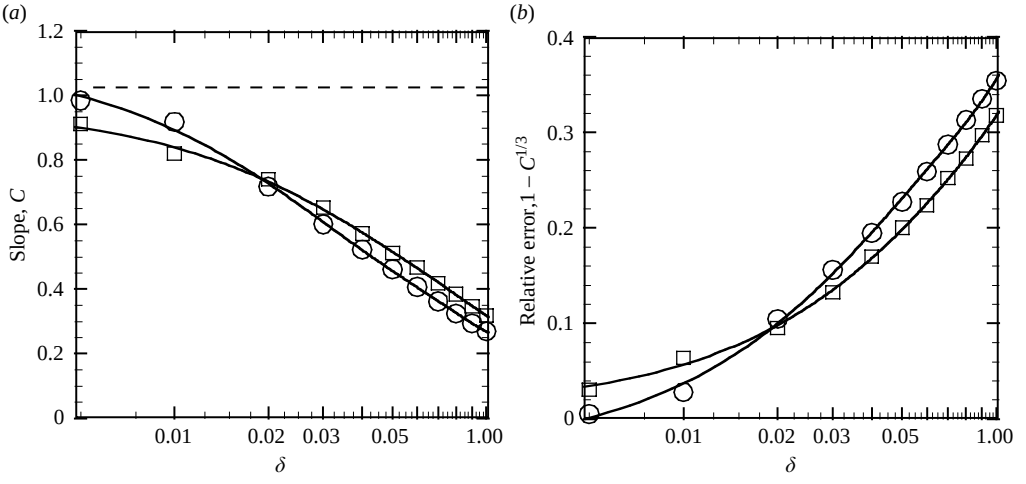

FIGURE 4. (*a*) Slope C from (12) and (*b*) relative error estimate $1 - C^{1/3}$ in dynamic contact angle for ○, $Bo = 0.02$; □, $Bo = 0.002$, as a function of precursor film thickness δ.

number cases are nearly identical. It is observed that the slope deviates significantly from unity for finite precursor film thicknesses, but seems to approach unity as $\delta \to 0$. The relative error in dynamic contact angle is approximately $1 - C^{1/3}$, which is plotted as a function of δ in figure 4(*b*). These results indicate that the disjoining pressure expression (4)–(5) yields quantitative agreement with the classical THV dynamic contact angle formula for $\delta \leqslant 0.01$ with a relative error in the contact angle of less than 5 %.

This validation study was repeated using the choice $(n, m) = (4, 3)$, and the predicted slope C and relative error $1 - C^{1/3}$ are compared with predictions of the $(n, m) = (3, 2)$

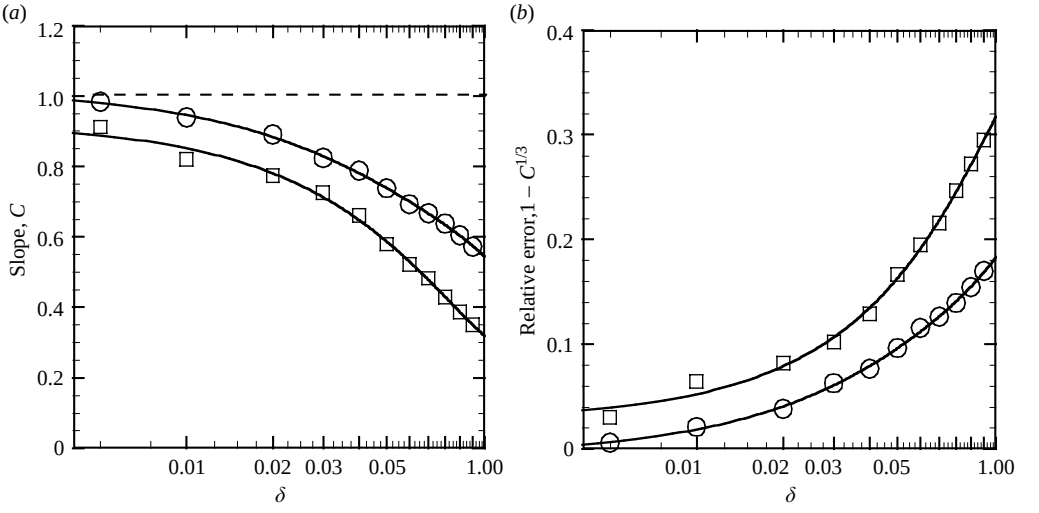

FIGURE 5. (*a*) Slope C from (12) and (*b*) relative error $1 - C^{1/3}$ for □, $(n, m) = (3, 2)$; ○, (4, 3).

case in figure 5, with Bond number of 0.02. The results indicate that the pair (4, 3) yields predictions significantly closer to the THV formula than the pair (3, 2) for a given value of δ; however, the computations are also significantly more prone to numerical instability. The reason for increase in accuracy for the choice (4, 3) over the choice (3, 2) is explained in the next section.

In addition to the above study of the equilibrium dynamic contact angle, we examined the transient response of the dynamic contact angle when the static contact angle is changed from one constant value to another. This test is performed by first allowing the film to attain an equilibrium form with a static contact angle $\theta_E = 0.1$. The computation is stopped and then restarted with a new static contact angle $\theta_E = 0.25$. The time variation of the dynamic contact angle following this sudden change in static contact angle is plotted in figure 6 for cases with $\delta = 0.01$, 0.05 and 0.1. When scaled by the final dynamic contact angle (for $\theta_E = 0.25$), the curves with different δ nearly collapse onto each other, which indicates that the characteristic response time of the dynamic contact angle upon a change in the static contact angle is nearly independent of precursor film thickness.

3.2. *Modified expression for the disjoining pressure coefficient B*

In this section, we derive an extension of the expression (5) for the disjoining pressure coefficient B which, with one empirically determined function, yields values of the slope C close to unity for values of δ as large as 0.1. Following Schwartz (1998), we examine a control volume (shown in figure 7) encompassing the region around the contact line, where the liquid film approaches the precursor film. On the left-hand side of this control volume (A), the film thickness has a value h_0, at which point the interface is assumed to approach a straight line with inclination angle θ_E. On the right-hand side of the control volume (B), the liquid film asymptotes to the precursor film, such that $h = h^*$ and the inclination angle vanishes. We further assume

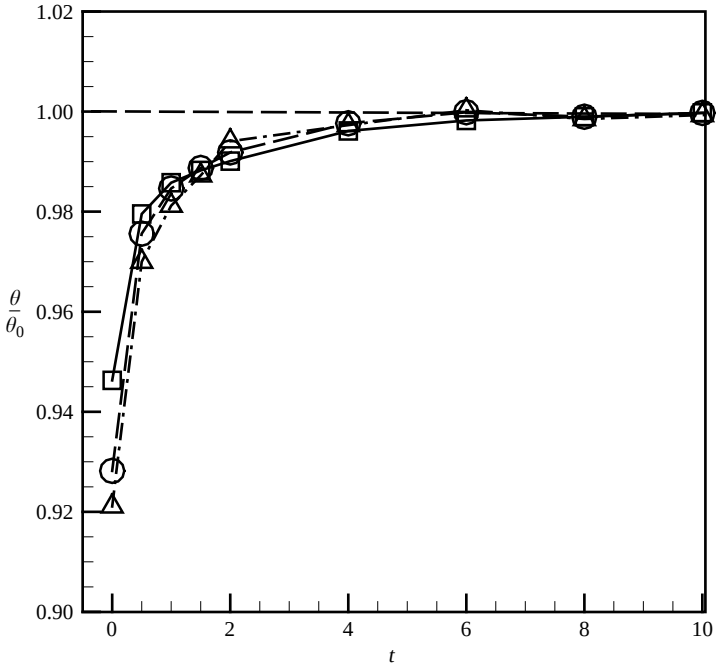

FIGURE 6. The transient response in normalized dynamic contact angle for □, $\delta = 0.01$; ○, 0.05; Δ, 0.1, from one equilibrium state with static contact angle $\theta_E = 0.1$ to a second equilibrium state with static contact angle $\theta_E = 0.25$.

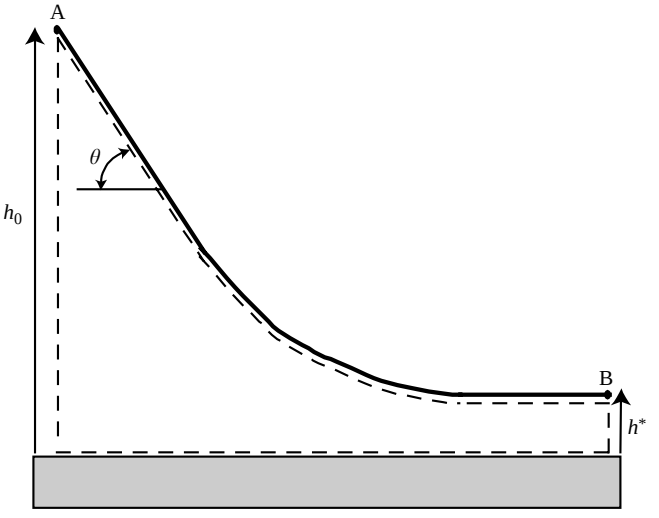

FIGURE 7. Control volume used in analysis to determine expression for disjoining pressure coefficient B.

that h_0 is sufficiently large compared to h^* that terms of $O(h^*/h_0)^2$ and higher are negligible. Unlike Schwartz, however, we retain terms of $O(h^*/h_0)$. Based on these assumptions, the second derivative $\partial^2 h/\partial x^2$ at A vanishes and the value of disjoining

pressure at A varies as $O(h^*/h_0)^m$, which is negligible for $m \geqslant 2$, so that from (3) the interfacial pressure in the liquid at A vanishes. Similarly, both the gradient of h and the disjoining pressure vanish at B, so the pressure must also vanish at B.

Integrating the liquid interfacial pressure from A to B yields

$$0 = \int_{h^*}^{h_0} \hat{p}(h)\,\mathrm{d}h = \sigma \int_{h^*}^{h_\infty} \sec^3\theta \left(\frac{\partial\theta}{\partial s}\right) \mathrm{d}h - \int_{h^*}^{h_\infty} \Pi\,\mathrm{d}h, \tag{13}$$

where we have used $\partial h/\partial x = \tan\theta$ and $\partial^2 h/\partial x^2 = -\sec^3\theta(\partial\theta/\partial s)$ and s is the arclength along the interface. Noting that $\mathrm{d}h/\mathrm{d}s = -\sin\theta$, we can rewrite this as

$$0 = -\sigma \int_{0^*}^{\theta_E} (\sin\theta)(\sec^3\theta)\,\mathrm{d}\theta - \int_{h^*}^{h_\infty} \Pi\,\mathrm{d}h. \tag{14}$$

Performing the indicated integration and using (4) yields

$$0 = \tfrac{1}{2}\sigma \tan^2\theta_E - Bh^*\left[\frac{n-m}{(m-1)(n-1)} - F\right], \tag{15}$$

where we define

$$F \equiv -\frac{1}{n-1}\left(\frac{h^*}{h_0}\right)^{n-1} + \frac{1}{m-1}\left(\frac{h^*}{h_0}\right)^{m-1}. \tag{16}$$

For the common choice $(n, m) = (3, 2)$, we have from (16) that

$$F \equiv \frac{h^*}{h_0} + O\left(\frac{h^*}{h_0}\right)^2. \tag{17}$$

If δ is sufficiently small, there might exist some value $h_0 \ll h_\infty$ such that $h^*/h_0 \ll 1$ and the factor F in (17) can be neglected; however, for values of δ that are small, but not infinitesimal, this factor must be retained. We note that for the choice $(n, m) = (4, 3)$, (16) indicates that $F \equiv O(h^*/h_0)^2$, so we would expect significantly less error for finite values of h^*/h_0. The results in figure 5 indeed indicate that this is the case.

Solving for B from (15) yields

$$B = f\frac{\sigma(m-1)(n-1)}{2h^*(n-m)} \tan^2\theta_E, \tag{18}$$

where we define

$$f \equiv \left[1 - \frac{F(m-1)(n-1)}{(n-m)}\right]^{-1}. \tag{19}$$

The expression (18) reduces to the expression (5) given by Schwartz (1998) to within $O(\theta_E^4)$ for the case with $f = 1$. However, we note that the factor F in (17) is subject to the lower bound $F \geqslant \delta$, since h_0 must be less than h_∞, which for the popular case $(n, m) = (3, 2)$ yields a restriction for the coefficient f as $f \geqslant 1/(1 - 2\delta)$. For δ in the interval $0.01 \leqslant \delta \leqslant 0.1$, the lower bound for f varies from 1.02 to about 1.25, which could lead to significant differences with predictions obtained using the expression (5).

In order to estimate the coefficient f in (19), we assume that the ratio h^*/h_0, and hence the factor f, can be expressed as a function of δ. To check this assumption, we repeat the plots of θ'^3 versus $\theta_E'^3$ and confirm that these plots are still linear for $f \neq 1$. For instance, figure 8 exhibits approximately linear variation of θ'^3 with $\theta_E'^3$ for a case with $\delta = 0.05$ for both $f = 1$ and $f = 1.55$, where the latter value of f (corresponding to $h^*/h_0 = 0.25$) yields $C = 1$ in (12), in agreement with the THV formula. The value

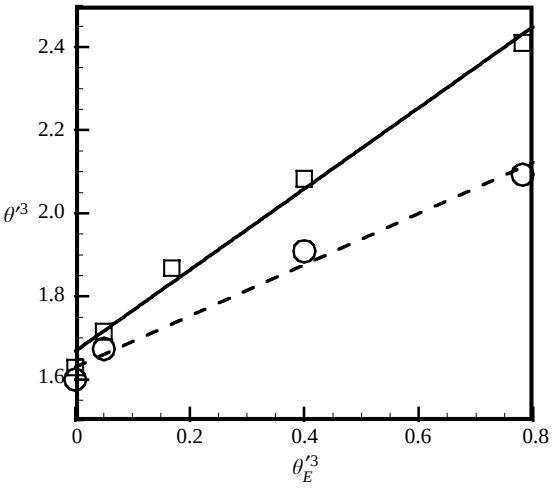

FIGURE 8. The linear variation of θ'^3 with $\theta_E'^3$ for $\delta = 0.05$ with - -○- -, $f = 1$; —□—, $f = 1.55$.

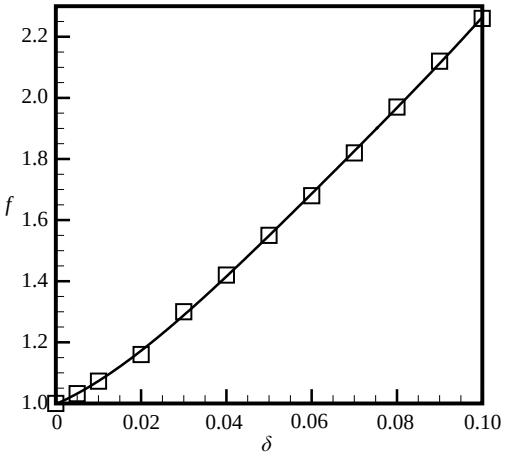

FIGURE 9. The values of the coefficient $f(\delta)$ that yield slope $C = 1$ in (12) □, along with the best fit polynomial expression given in (20).

of the coefficient f was similarly determined for each value of δ so as to make the slope $C = 1$, and the resulting values of f are plotted in figure 9. A polynomial fit to this data, given by

$$f(\delta) = 1 + 6.069\delta + 161.7\delta^2 - 1547\delta^3 + 5890\delta^4, \tag{20}$$

is plotted as a solid curve in figure 8. By selecting the coefficient f in accordance with the formula (20) and making the grid sufficiently fine to satisfy the restriction $\delta/\Delta x \geqslant 1.5$, we find that the dynamic contact angle varies in a manner consistent with the well-known THV formula when subjected to a change in static contact angle for values of δ up to 0.1.

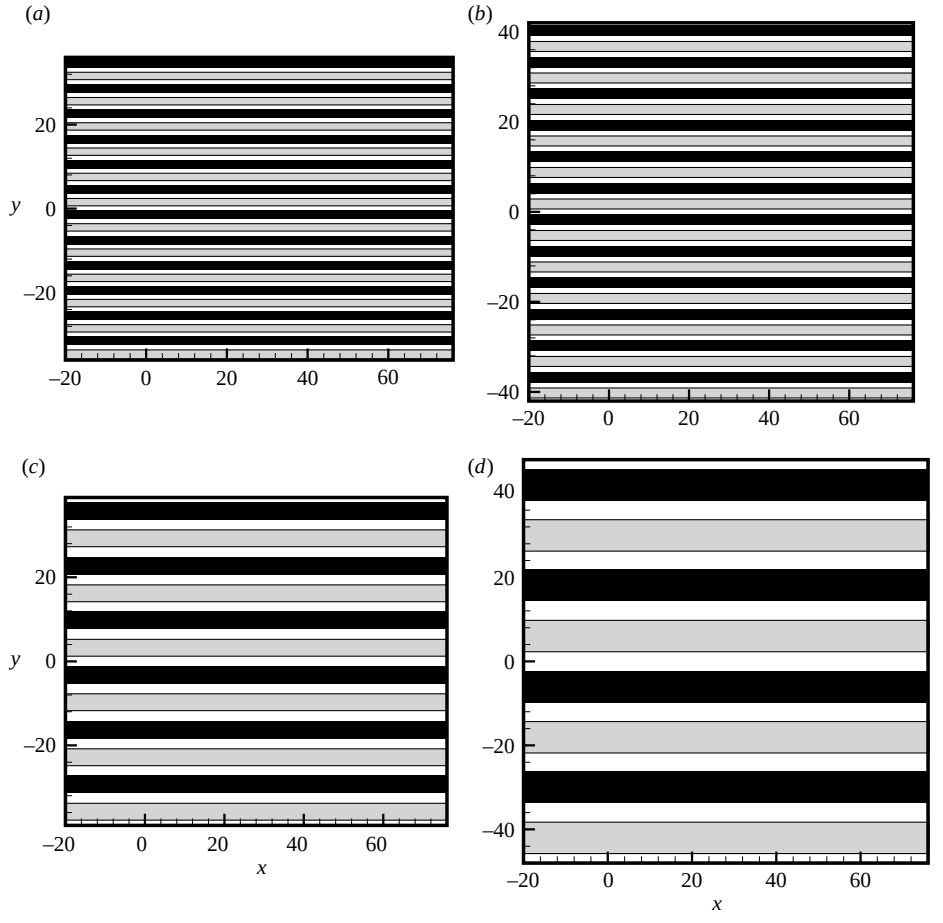

FIGURE 10. Contours of static contact angle for ordered strips with wavelength (*a*) $\lambda = 6$, (*b*) 7, (*c*) 13 and (*d*) 24. Grey shading indicates $\theta_E > 0.3$ and black shading indicates $\theta_E < 0.1$.

4. Results for static contact angle variation with ordered streamwise strips

The computational method described above is used in this section to examine the effect of streamwise strips of varying contact angle on the development of the fingering instability of a driven liquid film. The computation is performed with periodic boundary conditions in the y-direction and static contact angle variation given by

$$\theta_E(y) = \theta_{E,0}(1 + \varepsilon \sin(2\pi y/\lambda)], \tag{21}$$

with $\theta_{E,0} = 0.2$ and $\varepsilon = 0.9$. Static contact angle patterns are shown in figure 10 for cases with $\lambda = 6$, 7, 13 and 24. From figure 1(*b*), we find that the film front is stable for perturbations with $\lambda = 6$ and 7 (with growth rates $\beta = -0.49$ and -0.14, respectively), close to the most unstable case with $\lambda = 13$ ($\beta = 0.24$), and unstable with $\lambda = 24$ ($\beta = 0.14$).

The computations are performed with grid spacing $\Delta x = \Delta y = 0.03$ and precursor film thickness $\delta = 0.05$, yielding $\delta/\Delta x = 1.67$. The tests reported in § 3 indicate that the dynamic contact angle is nearly grid-independent for $\delta/\Delta x \geqslant 1.5$. The time step

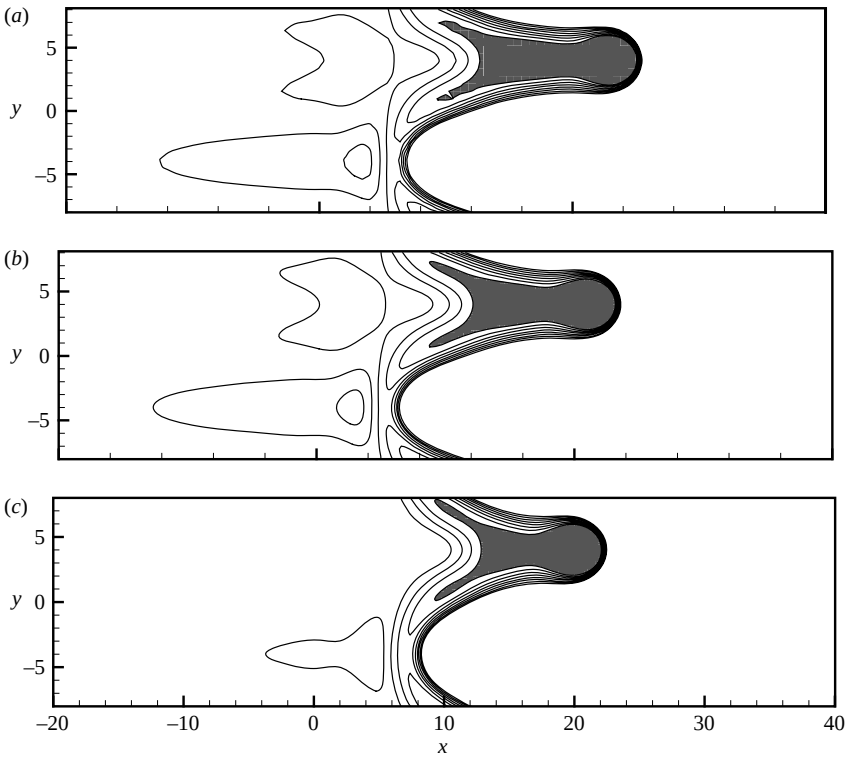

FIGURE 11. The effect of numerical resolution and precursor film thickness on the growth of a rivulet for a case with $\lambda = 16$ at time $t = 15$ for the three cases: (*a*) $\Delta t = 0.005$, $\Delta x = 0.03$, $\delta = 0.05$; (*b*) $\Delta t = 0.0025$, $\Delta x = 0.01$, $\delta = 0.05$; and (*c*) $\Delta t = 0.0025$, $\Delta x = 0.01$, $\delta = 0.03$. Eight contours of film thickness are plotted in the interval $h = (0.7,\ 1.3)$, with grey shading for $h > 1.3$.

was $\Delta t = 0.005$, and the total number of points was over 10 million. Results of a study of the effect of grid resolution and of the precursor film thickness on the rivulet development are given in figure 11, where we show contours of the film thickness for three different cases at time $t = 15$ and with strip wavelength $\lambda = 16$. The case shown in figure 11(*a*) corresponds to the numerical parameters used in the remainder of the computations ($\Delta x = 0.03$, $\Delta t = 0.005$, $\delta = 0.05$). A case with the same precursor film thickness but twice the grid spacing and twice the time step is shown in figure 11(*b*) ($\Delta x = 0.01$, $\Delta t = 0.0025$, $\delta = 0.05$). A case with the same grid and time step sizes as in figure 11(*b*), but with a smaller precursor film thickness ($\delta = 0.03$) is shown in figure 11(*c*). We observe that the cases with different numerical resolution, but the same precursor film thickness, in figures 11(*a*) and 11(*b*) exhibit very similar contours of film thickness. The case with smaller precursor film thickness in figure 11(*c*) exhibits slightly delayed growth and less pronounced fluctuations in the wake region behind the rivulet, but otherwise has similar shape and overall development. Since the fingering growth rate is known to be dependent on the value of the precursor film thickness (Kataoka & Troian 1997), it is not surprising that cases with different δ exhibit slight differences. However, in the range of δ used in the study, these differences clearly do not affect the qualitative film dynamics.

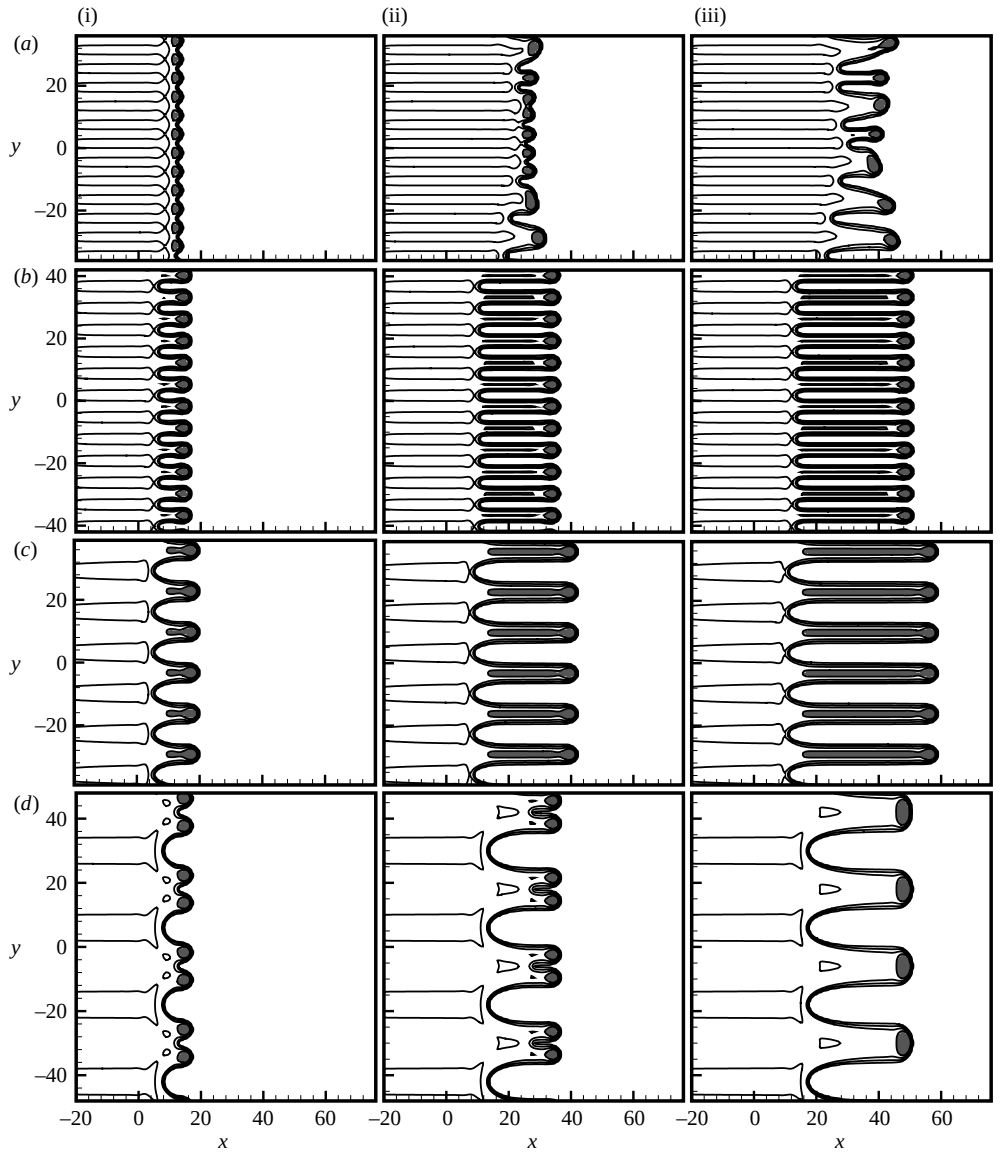

FIGURE 12. Contour plots of film thickness for cases with (*a*) $\lambda = 6$, (*b*) 7, (*c*) 13, and (*d*) 24, at times (i) $t = 12$, (ii) 24 and (iii) 33. (Time proceeds from left to right.) Contour lines are drawn for $h = 0.2$, 0.6, 1 and 1.4, with grey shading used for $h > 1.4$.

Contours of the film thickness are presented in figure 12 for the four values of λ given in figure 10, at times $t = 12$, 24 and 33. The different cases exhibit a number of interesting behaviours. Case (*a*) is well into the stable range, with $\beta = -0.49$, and thus develops only small-amplitude waves at the strip wavelength, $\lambda = 6$, which do not grow in time. However, as the front progresses downstream, these short waves merge to form waves with twice the wavelength. These longer waves are unstable according to linear theory and grow into rivulets by the end of the computation. A similar merger of neighbouring fingers was observed experimentally by Kataoka & Troian (1999) in their study of thermally driven films along parallel heated strips for a case with strip

width smaller than the critical width for the fingering instability. Case (*b*) is also for a wavelength which is stable according to linear theory (with $\beta = -0.14$). However, we nevertheless observe that waves with wavelength $\lambda = 7$ grow and develop into long thin rivulets. This type of subcritical instability, caused by nonlinear interactions forced by the surface imhomogeneities, was also observed by Marshall & Wang (2005) in computations with arrays of spots with different contact angle.

For Case (*c*), the wavelength is close to the most unstable wavelength, and we observe the expected rivulet growth at a wavelength corresponding to the strip wavelength. The length of the rivulets at the end of the computation is longest for this case, compared to any of the other cases examined, as would be expected. Case (*d*) is also unstable, but the strips are for a wavelength of about twice the most unstable wavelength. We initially observe the growth of perturbations with both the strip wavelength ($\lambda = 24$) and half the strip wavelength ($\lambda = 12$), which is close to the most unstable wave. The resulting structure in figure 12(*d*)(ii) looks rather like a rivulet with two heads located in each low contact-angle strip. These two heads eventually merge together, such that by the end of the computation (figure 12*d*(iii)) only a single rivulet head is evident in each strip. The forcing due to the strips of variable contact angle cause a type of lock-on phenomenon in this flow, leading to eventual growth of rivulets at the strip (or forcing) wavelength rather than the most unstable wavelength of the linear instability theory. This phenomenon is analogous to the lock-on phenomenon observed for other forced nonlinear vibration problems, such as for the problem of flow past a vibrating cylinder in which vortices are observed to shed into the cylinder wake at the cylinder vibration frequency rather than at the natural shedding frequency (Williamson & Govardhan 2004).

The maximum value of the change in film thickness, $\Delta h_{max}(t) \equiv \overset{max}{x,y}[h(x, y, t) - h_0(x, t)]$, is plotted versus time for these four cases in figure 13. All cases exhibit a rapid initial transient. In the two cases that are linearly stable (figures 13*a* and 13*b*), there is no linear part of the curve and the initial transient continues until the film saturates at a nearly constant film thickness within the 'head' region of the rivulet. In figure 13(*a*), there is jump in the maximum film thickness starting at about $t = 18$, which corresponds to the effect of merger of neighbouring stable perturbations to form unstable fingers with twice the wavelength. The two cases that are linearly unstable (figures 13*c* and 13*d*) both exhibit nearly linear growth in film thickness before saturating to a nearly uniform value. The growth rate predicted from the linear theory for a homogeneous surface is indicated by the slope of the dashed line in each of these figures for the corresponding value of λ. In both cases, we observe that the film thickness grows somewhat faster than the prediction of linear theory owing to the forcing from the surface contact angle variation.

Figure 14 shows the maximum value of film thickness on a line $y = \text{const}$ as a function of y for the same three times as shown in figure 12. The merger of neighbouring waves is evident from the wavelength doubling of the perturbations in figure 14(*a*)(iii). Cases with $\lambda = 7$ and 13 both reach an asymptotic film thickness fairly early, which does not change significantly as the rivulet grows in length. The case with $\lambda = 24$ exhibits two peaks within each contact angle strip, with a deep trough in film thickness in-between the two peaks. The film thickness increases substantially following the merger of these two rivulets (figure 14*d*(iii)).

Behind the rivulet front there remain strips with variable film thicknesses corresponding to the strips in static contact angle. Both the film thickness and the liquid flow rate vary nearly sinusoidally as one traverses across these strips, with thicker

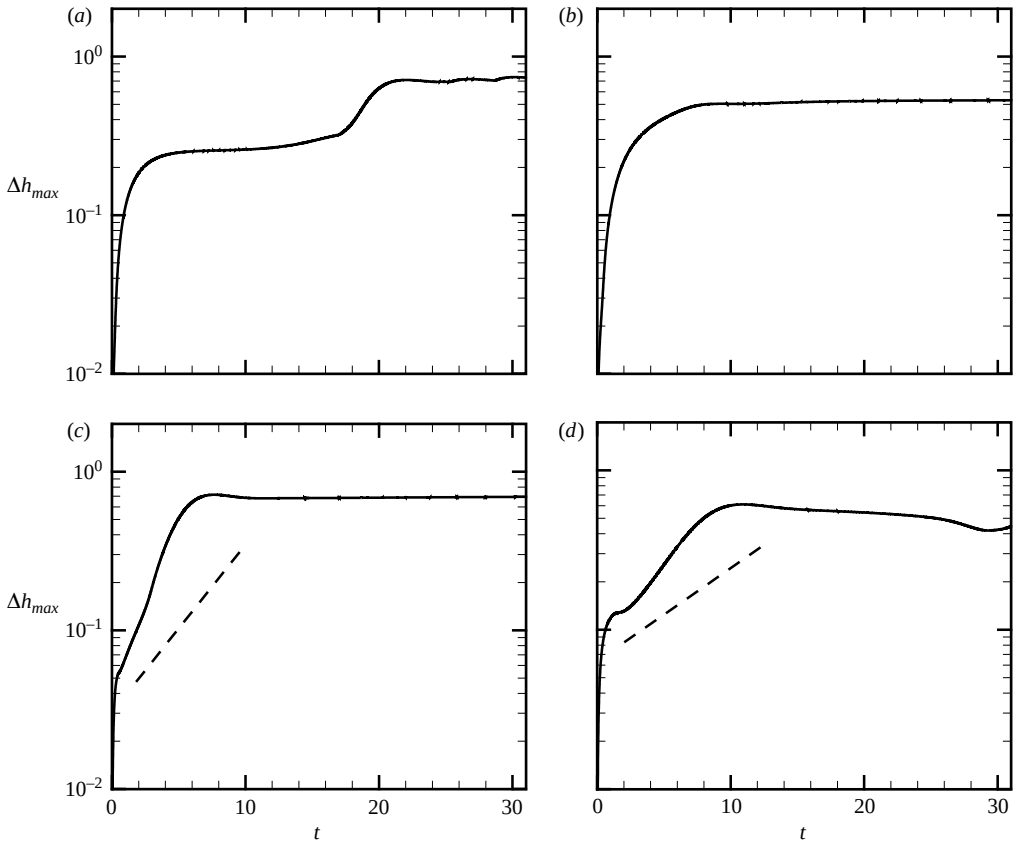

FIGURE 13. Maximum value of the change in film thickness as a function of time for the four cases shown in figure 12. The slope of the dashed line shows the predicted growth rate from linear stability theory for perturbations with wavelength λ. The linear stability theory predicts cases (*a*) and (*b*) are stable.

λ	6	7	13	24
$C(\Delta h, \Delta\theta_E)$	−0.965	−0.934	−0.822	−0.670
$C(Q, \Delta\theta_E)$	−0.962	−0.930	−0.83	−0.67
$C(\Delta h, Q)$	0.997	0.998	0.997	0.993
$rms(h)$	0.050	0.064	0.057	0.026
$rms(Q)$	0.145	0.185	0.163	0.075

TABLE 1. Correlations and root-mean-square variations of h and Q behind the rivulet front for cases with strips of variable static contact angle at $t = 33$.

strips corresponding to larger flow rate. At time $t = 33$, we present in table 1 the correlations between film thickness, flow rate and static contact angle for the region behind the rivulet front (corresponding to $x < 20$, $x < 5$, $x < 8$ and $x < 10$ for cases with $\lambda = 6$, 7, 13 and 24, respectively), as well as the root-mean-square (*rms*) values of the film thickness and flow rate in this region. The film thickness and the flow rate are nearly perfectly correlated. The static contact angle and the film thickness exhibit

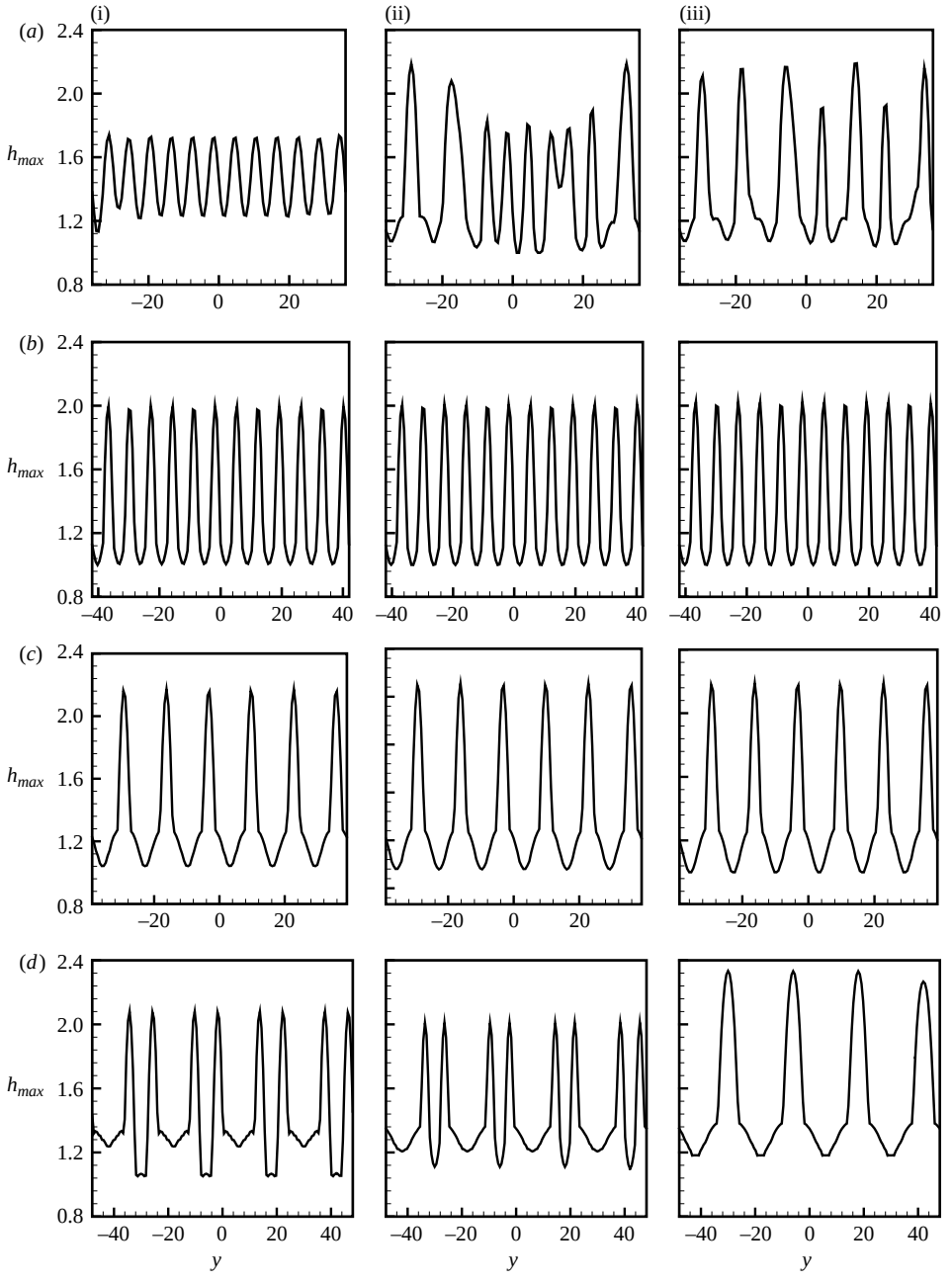

FIGURE 14. The maximum value of film thickness on a line $y = \text{const}$ as a function of y for the four cases and at the same times (i)–(iii) as shown in figure 12.

a strong negative correlation, with the strongest negative correlation for the smallest values of λ. In general, regions with large static contact angle have a thinner liquid film and smaller liquid flow rate than do regions with relatively smaller static contact angle. The root-mean-square variation in the region behind the rivulet front, due to the variation in static contact angle, is between 2.5 and 6.5 % of h and between 7 and 19 % of Q.

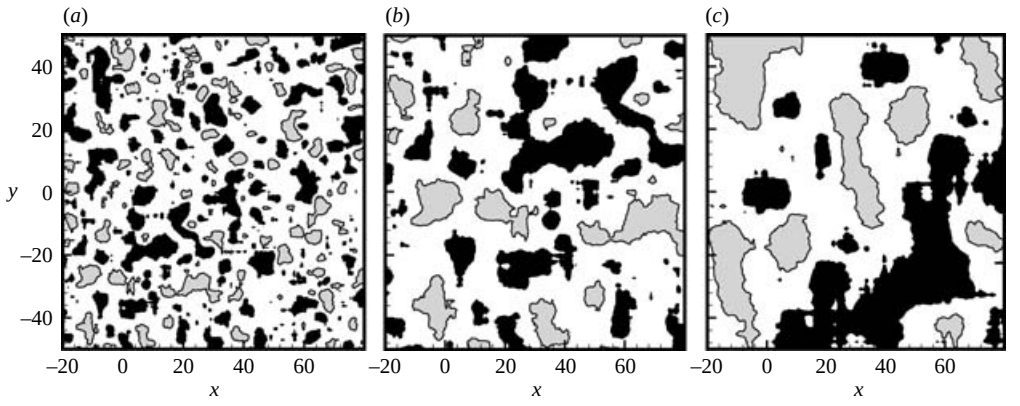

FIGURE 15. Contours of the static contact angle on random surfaces generated using correlation lengths (*a*) $\ell = 6$, (*b*) 13 and (*c*) 24. Grey shading indicates $\theta_E > 0.26$ and black shading indicates $\theta_E < 0.16$.

5. Results for random static contact angle variation

In order to mimic the heterogeneity typical of natural surfaces, we seek a random function with which to specify variation of the static contact angle. Even on a random surface, however, the variation of a function on the surface can be characterized in terms of one or more dominant length scales and the variance of the function autocorrelation. To examine the effect of surface heterogeneity on contact line stability and fingering typical of natural surfaces, we implemented a method developed by Hu & Tonder (1992) for generation of a two-dimensional random function $\phi(x, y)$. The value of the function $\phi(x, y)$ varies over the interval $(-1, 1)$ with standard deviation $\gamma = 0.245$ and autocorrelation given by

$$R(x, y) = \gamma^2 \exp[-\pi\{(x/\ell)^2 + (y/\ell)^2\}], \tag{22}$$

where ℓ is the correlation length. The static contact angle was then set using the random function $\phi(x, y)$ by

$$\theta_E(x, y) = \theta_{E,0}[1 + \varepsilon\phi(x, y)], \tag{23}$$

where the average contact angle $\theta_{E,0} = 0.2$ and the amplitude $\varepsilon = 0.9$. The resulting distribution for static contact angle $\theta_E(x, y)$ varies over the interval (0.02, 0.38) with standard deviation 0.044. Samples of random surfaces generated with correlation lengths of $\ell = 6$, 13 and 24 are shown in figure 15.

In the current computations, the homogeneous boundary conditions, (8*b*), are used in the y-direction and all other numerical parameters are the same as reported for the strip computation in § 4. Computations were performed for the three static contact angle fields shown in figure 15. Contours of film thickness for these three computations are shown in figure 16 at times $t = 12$, 24 and 33. Plots of maximum change in film thickness versus time are shown in figure 17, and plots of maximum film thickness on lines with $y = \text{const}$ are plotted versus y in figure 18. We observe much less dependence on static contact angle in the random surface computations than was reported for the surfaces with contact angle variation in strips in § 4. Rivulets grow

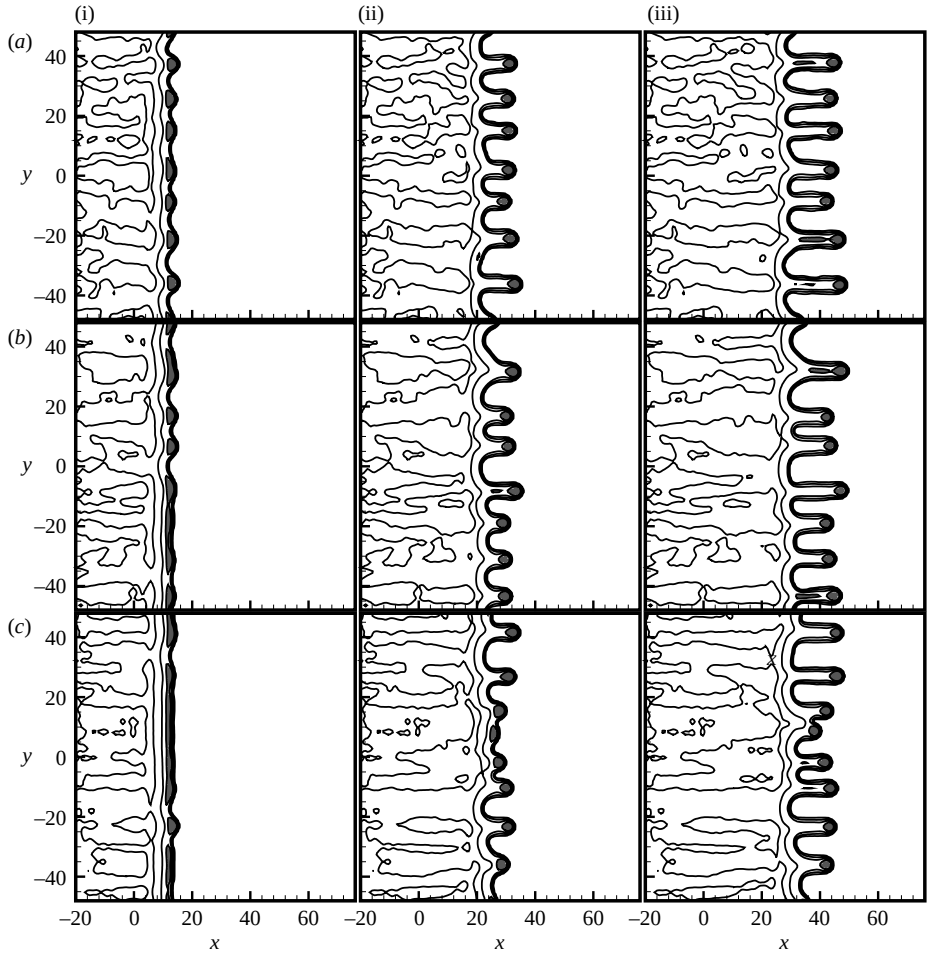

FIGURE 16. Contour plots of film thickness for cases with (*a*) $\ell = 6$, (*b*) 13, and (*c*) 24, at times (i) $t = 12$, (ii) 24 and (iii) 33. (Time proceeds from left to right.) Contour lines are drawn for $h = 0.2$, 0.6, 1 and 1.4, with grey shading used to $h > 1.4$.

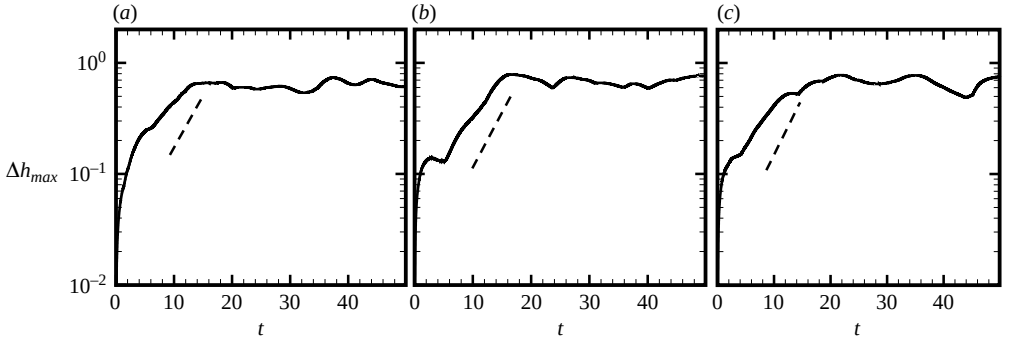

FIGURE 17. Maximum value of the change in film thickness as a function of time for the three cases shown in figure 16. The dashed line indicates the slope predicted by linear stability theory for the most unstable perturbation ($k = 0.48$).

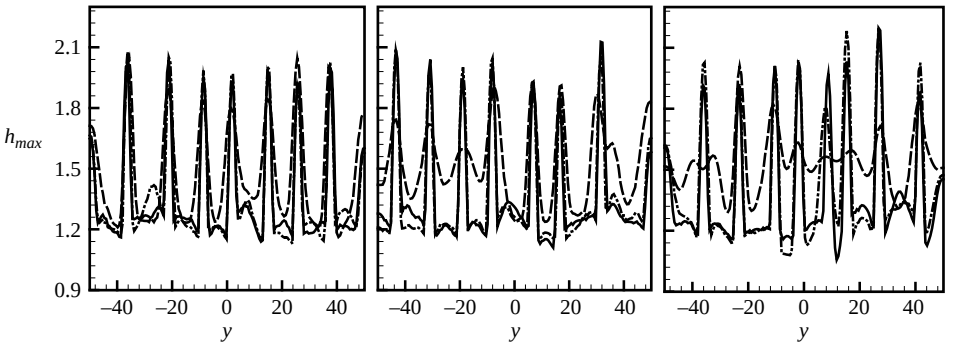

FIGURE 18. Plot showing the maximum value of film thickness on a line $y = \text{const}$ as a function of y for the three cases shown in figure 16. Results are given for - - -, $t = 12$; –·–, 24; —, 33.

λ	6	13	24
$C(\Delta h, \Delta\theta_E)$	−0.324	−0.256	−0.191
$C(Q, \Delta\theta_E)$	−0.249	−0.230	−0.168
$C(\Delta h, Q)$	0.947	0.978	0.974
$rms(h)$	0.011	0.0072	0.0056
$rms(Q)$	0.035	0.022	0.017

TABLE 2. Correlations and root-mean-square variations of h and Q behind the rivulet front for cases with random variation in static contact angle at $t = 33$.

in all three cases exhibited with about the same spacing, with mean value that seems to correspond well with the most unstable wavelength from linear theory, although with significant random variation about this mean spacing. While the mean rivulet spacing and length is about the same for all three cases, the case with the largest correlation length exhibits significantly more variation about the mean than does the case with the smallest correlation length. The rivulet growth rate is also nearly the same in all three cases, and is found to be slightly less than that of the most unstable wave from the linear theory, which is indicated by a dashed line in figure 17.

Behind each rivulet we observe a streak of fluid with slightly thicker film thickness, which marks the path that the rivulet has taken. Although these paths exhibit slight irregularities, they are for the most part straight, showing that the rivulets do not meander significantly owing to surface heterogeneity. Correlations between film thickness, liquid flow rate, and static contact angle in the region behind the rivulet front ($x < 25$) are recorded in table 2 for cases with random static contact angle variation at $t = 33$. As in the case discussed in § 4, we observe strong correlation between h and magnitude Q of the flow rate. However, the negative correlation between film thickness and static contact angle is much weaker than for the case with ordered strips of different static contact angle. Similarly, the root-mean-square values of h and Q are nearly an order of magnitude lower for the case with random static contact angle variation than for the case with ordered strips, even though the maximum and minimum values of the static contact angle are nearly the same for both cases. The main difference between the case of random contact angle examined in this section and that of ordered strips is that for the ordered strips, a liquid particle primarily sees one static contact angle it advects in the streamwise (x) direction. By contrast, for the case with random contact angle, a liquid particle sees a wide variety of static contact angles as it is advected by

the driving force. Consequently, the liquid film might start to grow thicker in a region of lower static contact angle, and then be driven into a region of larger static contact angle, in which it seeks to grow thicker. The constant change in static contact angle along the fluid pathline keeps the change in film thickness relatively smaller than for the ordered strip case and reduces the correlation between film thickness and static contact angle owing to the dependence of the film thickness on the history of the contact angle along the pathline.

6. Conclusions

The paper examines the effect of surface heterogeneity, as manifested by spatial variation of the static contact angle, on the dynamics of a driven liquid film. The static contact angle is controlled by a coefficient in the disjoining pressure term. We have shown that for sufficiently small values of the precursor film thickness ($\delta < 0.01$) and for sufficiently small grid increment ($\delta/\Delta x \geqslant 1.5$), this method for varying static contact angle yields predictions for dynamic contact angle that approach the values given by the classical Tanner–Hoffman–Voinov formula. Significant difference with this formula is observed for finite values of precursor film thickness; however, we have traced this difference back to an assumption in the derivation of the expression for the disjoining pressure coefficient and have shown how this coefficient can be corrected to yield close agreement with the Tanner–Hoffman–Voinov formula for finite values of the precursor film thickness. In addition to the study of equilibrium dynamic contact angle, the transient response of the dynamic contact angle is examined when the static contact angle is changed from one constant value to another constant value. We find that the characteristic response time of the dynamic contact angle following a change in the static contact angle is nearly independent of precursor film thickness.

The computational method is used to examine the effect of various patterns of surface heterogeneity on the development of the fingering instability of a driven liquid film, including streamwise strips of varying static contact angle and random variation of static contact angle. For cases with ordered strips of different static contact angles, the computations indicate that cases with λ greater than the critical wavelength from the linear stability theory develop perturbations at the strip spacing length, which over time grow into rivulets. The maximum film thickness initially increases until it saturates to a constant value as the rivulet forms. For cases with strip spacing distance λ that are much smaller than the critical wavelength for linear instability, a wavy pattern develops on the driven front with wavelength corresponding to the strip spacing. This wavy pattern advects in the streamwise-direction without significant growth until neighbouring waves merge, forming rivulets that grow with a wavelength twice that of the strip spacing. For values of strip-spacing distance slightly less than the critical value for linear instability, a subcritical instability is observed wherein rivulets form and grow owing to nonlinear effects driven by forcing from the surface heterogeneities. When the strip spacing is much larger than the most unstable wave from linear theory, we observe multiple rivulets to form initially in each strip at close to the most unstable wavelength from linear stability theory, where these fingers later merge to form rivulets whose wavelength equals that of the strip spacing. Some of these same effects have also been observed for films driven over grooved surfaces (Kondic & Diez 2002).

We also examine fingering and rivulet development on three surfaces with random static contact angle variation, but with different correlation lengths. These cases all exhibit rivulet formation with about the same mean spacing and length, both of which

are roughly equal to what would be predicted for the fastest-growing wave from the linear theory. However, cases with large correlation length exhibit significantly more variation around the mean rivulet spacing and length than do cases with small correlation length.

The paper demonstrates that the precursor film method with disjoining pressure can be used for accurate prediction of film dynamics problems with variable contact angle. We find that engineered surfaces with strips of contact angle variation can have a significant influence on the film dynamics and the spacing of the rivulets, in some cases inducing rivulets to form with a spacing that is prohibited by linear theory. We find that random variation in contact angle has a much milder effect on the rivulet development than do streamwise strips. However, limitations of the numerical model did not allow us to extend the computations to cases with very large contact angle variation, for which the effect of the random contact angle patterns may have been more pronounced.

Financial support is provided by the NASA Office of Biological and Physical Research under grant number NAG3-2368. Dr Charles Neiderhaus is the project monitor.

REFERENCES

Bertozzi, A. L. & Brenner, M. P. 1997 Linear stability and transient growth in driven contact lines. *Phys. Fluids* **9**, 530–539.

de Bruyn, J. R. 1992 Growth of fingers at a driven three-phase contact line. *Phys. Rev.* A **46**, R4500–R4503.

Cazabat, A. M., Heslot, F., Troian, S. M. & Carles, P. 1990 Fingering instability of thin spreading layers driven by temperature gradients. *Nature* **346**, 824–826.

Davis, J. M. & Troian, S. M. 2003 On a generalized approach to the linear stability of spatially nonuniform thin film flows. *Phys. Fluids* **15**, 1344–1347.

Davis, J. M. & Troian, S. M. 2004 Influence of boundary slip on the optimal excitations in thermocapillary driven spreading. *Phys. Rev.* E **70**, 046309-1–046309-11.

Diez, J. A. & Kondic, L. 2001 Contact-line instabilities on thin liquid films. *Phys. Rev. Lett.* **86**, 632–635.

Diez, J. A., Kondic, L. & Bertozzi, A. 2000 Global models for moving contact lines. *Phys. Rev.* E **63**, 011208-1–011208-13.

Eres, M. H., Schwartz, L. W. & Roy, R. V. 2000 Fingering phenomena for driven coating layers. *Phys. Fluids* **12**, 1278–1295.

Fraysse, N. & Homsy, G. M. 1994 An experimental study of rivulet instabilities in centrifugal spin coating of viscous Newtonian and non-Newtonian fluids. *Phys. Fluids* **6**, 1491–1504.

Garnier, N., Grigoriev, R. O. & Schatz, M. F. 2003 Optical manipulation of microscale fluid flow. *Phys. Rev. Lett.* **91**, 054501-1–054501-4.

de Gennes, P. G. 1985 Wetting: statics and dynamics. *Rev. Mod. Phys.* **57**, 827–863.

Golovin, A. A., Rubinstein, B. Y. & Pismen, L. M. 2001 Effect of van der Waals interactions on the fingering instability of thermally driven thin wetting films. *Langmuir* **17**, 3930–3936.

Greenspan, H. P. 1978 On the motion of a small viscous droplet that wets a surface. *J. Fluid Mech.* **84**, 125–143.

Grigoriev, R. O. 2003 Contact line instability and pattern selection in thermally driven liquid films. *Phys. Fluids* **15**, 1363–1374.

Hocking, L. M., Debler, W. R. & Cook, K. E. 1999 The growth of leading-edge distortions on a viscous sheet. *Phys. Fluids* **11**, 307–131.

Hoffman, R. L. 1975 A study of the advancing interface. Part 1. Interface shape in liquid–gas systems. *J. Colloid Interface Sci.* **50**, 228–241.

Hu, Y. Z. & Tonder, K. 1992 Simulation of 3-D random rough surface by 2-D digital filter and Fourier analysis. *Intl J. Machine Tools Manufact.* **32**, 83–90.

Huppert, H. E. 1982 Flow and instability of a viscous current down a slope. *Nature* **300**, 427–429.

Johnson, M. F. G., Schluter, R. A., Miksis, M. J. & Bankoff, S. G. 1999 Experimental study of rivulet formation on an inclined plate by fluorescent imaging. *J. Fluid Mech.* **394**, 339–354.

Kalliadasis, S. 2000 Nonlinear instability of a contact line driven by gravity. *J. Fluid Mech.* **413**, 355–378.

Kataoka, D. E. & Troian, S. M. 1997 A theoretical study of instabilities at the advancing front of thermally driven coating layers. *J. Colloid Interface Sci.* **192**, 350–362.

Kataoka, D. E. & Troian, S. M. 1999 Patterning liquid flow on the microscopic scale. *Nature* **402**, 794–797.

Kondic, L. & Diez, J. 2001 Pattern formation in the flow of thin layers down an incline: Constant flux configuration. *Phys. Fluids* **13**, 3168–3184.

Kondic, L. & Diez, J. 2002 Flow of thin films on patterned surfaces: controlling the instability. *Phys. Rev.* E **65**, 045301-1–045301-4.

López, P. G., Miksis, M. J. & Bankoff, S. G. 1997 Inertial effects on contact line instability in the coating of a dry inclined plate. *Phys. Fluids* **9**, 2177–2183.

Marshall, J. S. & Wang, S. 2005 Contact-line fingering and rivulet formation in the presence of surface contamination.*Comput. Fluids* **34**, 664–683.

Melo, F., Joanny, J. F. & Fauve, S. 1989 Fingering instability of spinning drops. *Phys. Rev. Lett.* **63**, 1958–1961.

Mohanty, K. K. 1981 Fluids in porous media: two-phase distribution and flow. PhD dissertation, University of Minnesota.

Moyle, D. T., Chen, M.-S. & Homsy, G. M. 1999 Nonlinear rivulet dynamics during unstable wetting flows. *Intl J. Multiphase Flow* **25**, 1243–1262.

Schwartz, L. W. 1998 Hysteric effects in droplet motions on heterogeneous substrates: Direct numerical simulation. *Langmuir* **14**, 3440–3453.

Schwartz, L. W. & Eley, R. R. 1998 Simulation of droplet motion on low-energy and heterogeneous surfaces. *J. Colloid Interface Sci.* **202**, 173–188.

Spaid, M. A. & Homsy, G. M. 1996 Stability of Newtonian and viscoelastic dynamic contact lines. *Phys. Fluids* **8**, 460–477.

Tanner, L. H. 1979 The spreading of silicone oil drops on horizontal surfaces. *J. Phys.* D: *Appl. Phys.* **12**, 1473–1484.

Thompson, B. E. & Marrochello, M. R. 1999 Rivulet formation in surface-water flow on an airfoil in rain. *AIAA J.* **37**, 45–49.

Troian, S. M., Herbolzheimer, F., Safran, S. A. & Joanny, J. F. 1989 Fingering instabilities of driven spreading layers. *Europhys. Lett.* **10**, 25–30.

Voinov, O. V. 1976 Hydrodynamics of wetting. *Izv. Akad. Nauk SSSR, Mekh. Zhid. i Gaza* **5**, 76–81.

Williamson, C. H. K. & Govardhan, R. 2004 Vortex-induced vibrations. *Annu. Rev. Fluid Mech.* **36**, 413–455.

Witelski, T. P. & Bowen, M. 2003 ADI schemes for higher-order nonlinear diffusion equations. *Appl. Numer. Math.* **45**, 331–351.